# Impact of crystal structure and defect on the electric properties in (LiCeY)-doped $CaBi_2Nb_2O_9$-based high-temperature piezoceramics

Jing Yuan[1] · Rui Nie[1] · Wan Li[1] · Jianguo Zhu[1]

## Abstract

The $Ca_{1-2x}(LiCe_{0.5}Y_{0.5})_xBi_2Nb_2O_9$ (CBNLCY-100x, x = 0–0.07) high-temperature ceramics were prepared by the conventional solid state reaction. The LiCeY substitution at A-site led an improvement of octahedral tilt angle in the *a–c* plane of CBNLCY-100x ceramics, which resulted in an enhanced piezoelectric constant. CBNLCY-6 ceramic with high Curie temperature ($T_C$ = 940 °C) had a high piezoelectric coefficient ($d_{33}$) of 16.3 pC/N, even after annealing at 800 °C for 2 h, the $d_{33}$ value of CBNLCY-6 ceramic still remained 92.6% of its original value. Furthermore, the *dc* conduction mechanism of the ceramics was studied. The oxygen vacancies played an important role in *dc* conduction mechanism at low temperature and the main conduction mechanism at high temperature was intrinsic conduction. The resistivity of CBNLCY-100x ceramics got highest value at x = 0.01 and the resistivity of CBNLCY-1 ceramic enhanced one order of magnitude compared with undoped $CaBi_2Nb_2O_9$ ceramic. These results suggest that the CBNLCY-6 ceramic is a promising candidate material for ultra-high temperature applications.

## 1 Introduction

Calcium bismuth niobate ($CaBi_2Nb_2O_9$, CBN) is one of the compounds in bismuth layer-structured ferroelectric (BLSF) family with a vast potential for applications in high temperature environment [1]. It exhibits excellent performance such as high Curie temperature ($T_C$ = 930 °C) and thermal stability [2], which make it useful over a wide temperature range. And it also possesses high resistivity and excellent fatigue-resistant properties. However, the piezoelectric activity ($d_{33} \sim 6$ pC/N) of CBN ceramics is very low due to the high coercive field ($E_c$) and the structural anisotropy [3], which limits its application in devices. The crystal structure of CBN ceramics is built of the interleaving $(CaNb_2O_7)^{2-}$ perovskite-like layers between with $(Bi_2O_2)^{2+}$ sheets that are stacked along its crystallographic *c*-direction, where A-site ion is $Ca^{2+}$ ion and B-site ion is $Nb^{5+}$ ion [4, 5].

In order to improve piezoelectric property of CBN ceramics, solid solutions with other ions substitution have been

considered and explored. For example, it is excepted to improve piezoelectric activity by doping with rare earth ions, alkali metal ions or combined of them at A-site and transition metal ions at B-site. Relative investigations mainly are listed in Table 1 [6–13]. It is clear that the piezoelectric properties of CBN ceramics were enhanced significantly by doping different ions. And in order to explain the electric properties of piezoelectric ceramics, the formation process and action mechanism of defect dipoles have been studied. Chen et al. [14] studied the effect of defect dipoles on dielectric relaxation and ferroelectric properties of W/Cr co-doped $Bi_4Ti_3O_{12}$ ceramics. Long and Fan [15] reported the double-loop-like ferroelectric polarization in acceptor Aurivillius ceramic and a positive polarization contribution from defect polarization. The similar studies were previously observed in typical perovskite ferroelectrics, e.g., Cu-doped $K_{0.5}Na_{0.5}NbO_3$ ceramics [16], Mg-doped $K_{0.5}Na_{0.5}NbO_3$ ceramics [17] and Mn-doped $Bi_{0.5}Na_{0.5}TiO_3$ ceramics [18]. In addition, the grain orientation techniques, such as template grain growth (TGG) [19] and spark plasma sintering (SPS) [20], can also improve the piezoelectricity of CBN ceramics effectively.

It is presented in Table 1 that the alkali metal ions and rare earth ions co-doping, especially lithium and cerium ions co-doping could improve the piezoelectric properties of BLSF ceramics well. But doping cerium ions ($Ce^{3+}$ or

✉ Jianguo Zhu
  nic0400@scu.edu.cn

  Jing Yuan
  yuanjingscu@163.com

[1] College of Materials Science and Engineering, Sichuan University, Chengdu 610064, People's Republic of China

**Table 1** Piezoelectric properties ($d_{33}$) and Curie temperature ($T_C$) of modified $CaBi_2Nb_2O_9$ ceramics prepared by solid state method

| Composition | $d_{33}$ (pC/N) | $T_C$ (°C) | References |
|---|---|---|---|
| $Ca_{0.95}La_{0.05}Bi_2Nb_2O_9$ | 12.8 | 911 | Reece et al. [6] |
| $Ca_{0.88}(LiCe)_{0.04}Bi_2Nb_2O_9$ | 13.3 | 960 | Tian et al. [7] |
| $Ca_{0.9}(Li_{0.5}Ce_{0.25}Pr_{0.25})_{0.1}Bi_2Nb_2O_9$ | 17.3 | 939 | Chen et al. [8] |
| $Ca_{0.9}(KCe)_{0.05}Bi_2Nb_2O_9$ | 16 | 868 | Wang et al. [9] |
| $Ca_{0.88}(LiCe)_{0.04}Bi_2Nb_{1.96}W_{0.04}O_9$ | 16.1 | 925 | Zhu et al. [10] |
| $Ca_{0.775}Sr_{0.025}(Li_{0.5}Ce_{0.15}Bi_{0.35})_{0.2}Bi_2Nb_{1.94}Ta_{0.04}W_{0.02}O_9$ | 17.5 | 917 | Chen et al. [11] |
| $Ca_{0.95}Li_{0.02}Nd_{0.02}O_{0.01}Bi_2Nb_{1.98}Sc_{0.01}W_{0.01}O_{8.985}$ | 20.6 | 908 | Long et al. [12] |
| $Ca_{0.80}(Li_{0.5}Ce_{0.15}Bi_{0.35})_{0.20}Bi_2Nb_2O_9$ | 17.2 | 928 | Chen et al. [13] |

$Ce^{4+}$) into CBN ceramics would decrease the Curie temperature of the ceramics and limit the application in high temperature environment. While the yttrium ions ($Y^{3+}$) have small ionic radii ($R_Y^{3+} = 1.25$ Å) and are helpful for increasing Curie temperature of the ceramics. So in this work, the $Ca_{1-2x}(LiCe_{0.5}Y_{0.5})_xBi_2Nb_2O_9$ (CBNLCY-100$x$) ceramics were prepared by solid state reaction and the crystal distortion and defect of CBNLCY-100$x$ ceramics are studied in detail to explain the enhanced piezoelectric constant, high Curie temperature and good thermal stability of the ceramics.

## 2 Experiments

$Ca_{1-2x}(LiCe_{0.5}Y_{0.5})_xBi_2Nb_2O_9$ (CBNLCY-100$x$, $x = 0$–0.07) ceramics were prepared by solid state reactions, using $CaCO_3$ (99%), $Bi_2O_3$ (99.999%), $Nb_2O_5$ (99.5%), $Li_2CO_3$ (99.99%), $CeO_2$ (99.99%) and $Y_2O_3$ (99.5%) as raw materials. All powders were weighed according to the stoichiometric compositions. After ball milling with zirconia balls for 12 h, the mixed powders were dried and calcined at 900 °C for 3 h, and then the mixtures were ball-milled again for 12 h. The powders were pressed into disks of 10 mm in diameter and 0.8 mm in thickness by 8 wt% polyvinyl alcohol (PVA) under 10 MPa. After burning off PVA at 450 °C, these disks were sintered at 1080 °C–1160 °C for 3 h. All the samples were poled at 180 °C in a silicone oil bath by applying a direct current electric field of ~ 12 kV/mm for 10 min.

The crystal structures were determined using the X-ray diffraction (XRD) with Cu-$K_\alpha$ radiation (DX2700, Dandong, China) at room temperature. The test was conducted by 0.02° scan step and continuous scanning type in the $2\theta$ range of 20°–60°. The powder X-ray diffraction data of CBNLCY-0 and CBNLCY-6 ceramics were collected from an automated diffractometer (Panalytical B.V. X'pert Pro) in a range of 20° to 120°. The temperature dependence of dielectric behavior of all samples were measured with an LCR analyzer (HP4980A, Agilent, USA). Their piezoelectric constant ($d_{33}$) was measured using a Belincourt meter (ZJ-3A, Institute of Acoustics, Chinese Academy of Sciences,

China). The *dc* resistivity was measured at high temperature by an electrometer (Keithley 6517B). Ferroelectric properties were determined out at room temperature using an aixACCT TF 2000 analyzer.

## 3 Results and discussion

Figure 1a shows the X-ray diffraction (XRD) of CBNLCY-100$x$ ceramics in the $2\theta$ range of 20°–60°. The analysis for diffraction peaks indicates that the major phase of all compositions can be indexed by PDF card (PDF#49–0608, $CaBi_2Nb_2O_9$). It is also found that there is less $Bi_2O_3$ (PDF 01-074-2351) existing in the matrix as the secondary phase. The formation of secondary phase $Bi_2O_3$ is due to the volatilization of bismuth element during sintering process. In the cooling process, the bismuth element reacts with oxygen to form bismuth oxide. Except $Bi_2O_3$ phase, there is only $CaBi_2Nb_2O_9$ phase indicates the doping ions ($Li^+$, $Ce^{4+}$, $Y^{3+}$) diffused into the lattice and formed a solid solution successfully. Figure 1b is the enlarged graph of XRD patterns in the range of 28°–30°. The highest intensity of diffraction peak is found to be (115), which is in accordance with the strongest diffraction peak (112$\underline{m}$ + $\underline{1}$) in BLSFs ceramics. Moreover, the (115) peak shifts to a high angle due to the substitution of smaller ions ($R_{Li}^+ = 1.15$ Å, $R_{Ce}^{4+} = 1.14$ Å, $R_Y^{3+} = 1.25$ Å, 12 CN) [21] for larger ions ($R_{Ca}^{2+} = 1.34$ Å, 12 CN) [22] in the A-site. The XRD diffraction peaks located at (200)/(020) are shown in Fig. 1c. It is clear that the (200) and (020) peaks tend to merge into a single peak with $x$ content increasing, which demonstrates the enhancement of lattice symmetry of CBNLCY-100$x$ ceramics [23].

In order to confirm the lattice parameters *a, b, c* and characterize the crystal structural conversion of CBNLCY-100$x$ ceramics, Rietveld refinements on powder XRD of CBNLCY-0 and CBNLCY-6 ceramics were refined using the MAUD program [24]. Figure 2a and c show the experimental and calculated XRD patterns for ceramics, the Bragg-position, and the difference between calculated and experimental intensity. The refined factors sig and $R_{wp}$, which are used to denote the quality of structural refinement, are 1.32,

**Fig. 1** XRD patterns of CBN-LCY-100$x$ ceramics: **a** 20°–60°; **b** 28°–30°; **c** 35°–37°
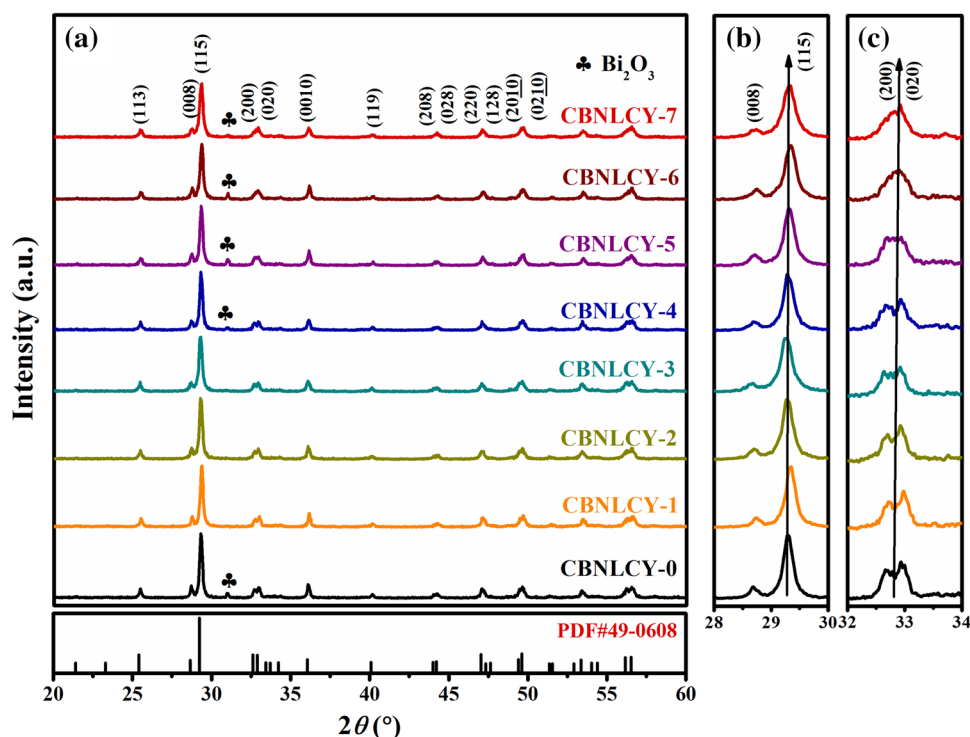


8.53 for CBNLCY-0 1.16, 8.14 for CBNLCY-6 respectively, indicating a good match between the observed and calculated patterns. Figure 2b and d are the enlarged XRD patterns located at (200)/(020). It is clear that the (200) and (020) peaks tend to merge into a single peak with $x$ content increasing and the ratio of $a/b$ value decreases from 1.008 to 1.0048 [25]. The variation indicates that the crystal structure undergoes a phase transition from orthorhombic phase to pseudo-tetragonal phase with the introduction of dopants [26]. It implies that crystal symmetry is enhanced by the compositional variation.

The visualized crystal structures of CBNLCY-0 and CBNLCY-6 ceramics shown in Fig. 3 are obtained from refinement results. It is reported that the main crystal distortion of BLSFs ceramics occurs in $NbO_6$ octahedron [27]. So the distortion of $NbO_6$ octahedron is deeply studied. The difference between Nb–O bond lengths in $NbO_6$ octahedron are decreases with the introduction of LiCeY, which implies the enhancement of octahedral symmetry. Besides, the octahedral tilt angles ($\alpha$) from $c$ axis of CBNLCY-0 and CBNLCY-6 ceramics are about 17.28° (Nb-O1-Nb bond angle: 145.45°) and 13.31° (Nb-O1-Nb bond angle: 153.39°) respectively. The decreasing tilt angle demonstrates the declining crystal distortion of CBNLCY-100$x$ ceramics, which can also explain the variation of (200) and (020) peaks in Fig. 2b and d. In order to describe the tilt angle along $a$ and $b$ axis, the tilt angle in the $a$–$c$ plane ($\alpha_x$) and in the $b$–$c$ plane ($\alpha_y$) are listed in Table 2. It is reported that the crystal distortion related to $\alpha_y$ do not contribute to the

spontaneous polarization ($P_s$). The results are attributed to the glide plane perpendicular to the $b$ axis which eliminates the ion displacement along $b$ axis [28]. Although tilt angle ($\alpha$) from $c$ axis decreases, the tilt angle in the $a$–$c$ plane increases from 1.03° to 15.82° as LiCeY content increase. The extent of octahedral rotation can be described by the rotation angle along $b$ axis in $a$–$b$ plane ($\beta_1$ and $\beta_2$) shown in Fig. 3. The rotation angles of CBNLCY-0 are 4.37° and 7.42°, and those of CBNLCY-6 are 4.72° and 5.82°. The change of the rotation angle is not obvious. This result indicates that the rotation of $NbO_6$ octahedron did not make the main contribution to the ferroelectricity of CBNLCY-100$x$ ceramics. Therefore, the enhanced lattice distortion related to $\alpha_x$ is responsible for the larger $P_s$.

Figure 4 shows the polarization–electric ($P$–$E$) loops and current–electric field ($I$–$E$) curves of CBNLCY-0 and CBNLCY-6 ceramics measured at 180 °C and 1 Hz. It can be seen that the $P$–$E$ loop of CBNLCY-0 ceramic exhibited cigar-shaped profile and there are no apparent ferroelectric switching peaks observed in the $I$–$E$ curve during the polarization process. With the substitution of LCY dopants, the remnant polarization $P_r$ and coercive field $E_c$ of the ceramcis obviously vary. The $P_r$ and $E_c$ of CBNLCY-0 ceramic are 0.51 μC/cm$^2$ and 3.66 kV/mm, respectively. While those of CBNLCY-6 ceramic are 1.35 μC/cm$^2$ and 6.94 kV/mm, respectively. The enhancement of $P_r$ is attribution to the larger $P_s$ of CBNLCY-6 ceramic which has discussed in crystal structure analysis. Hence, the LCY doping can improve the ferroelectric properties of CBN ceramics. Figure 5 shows
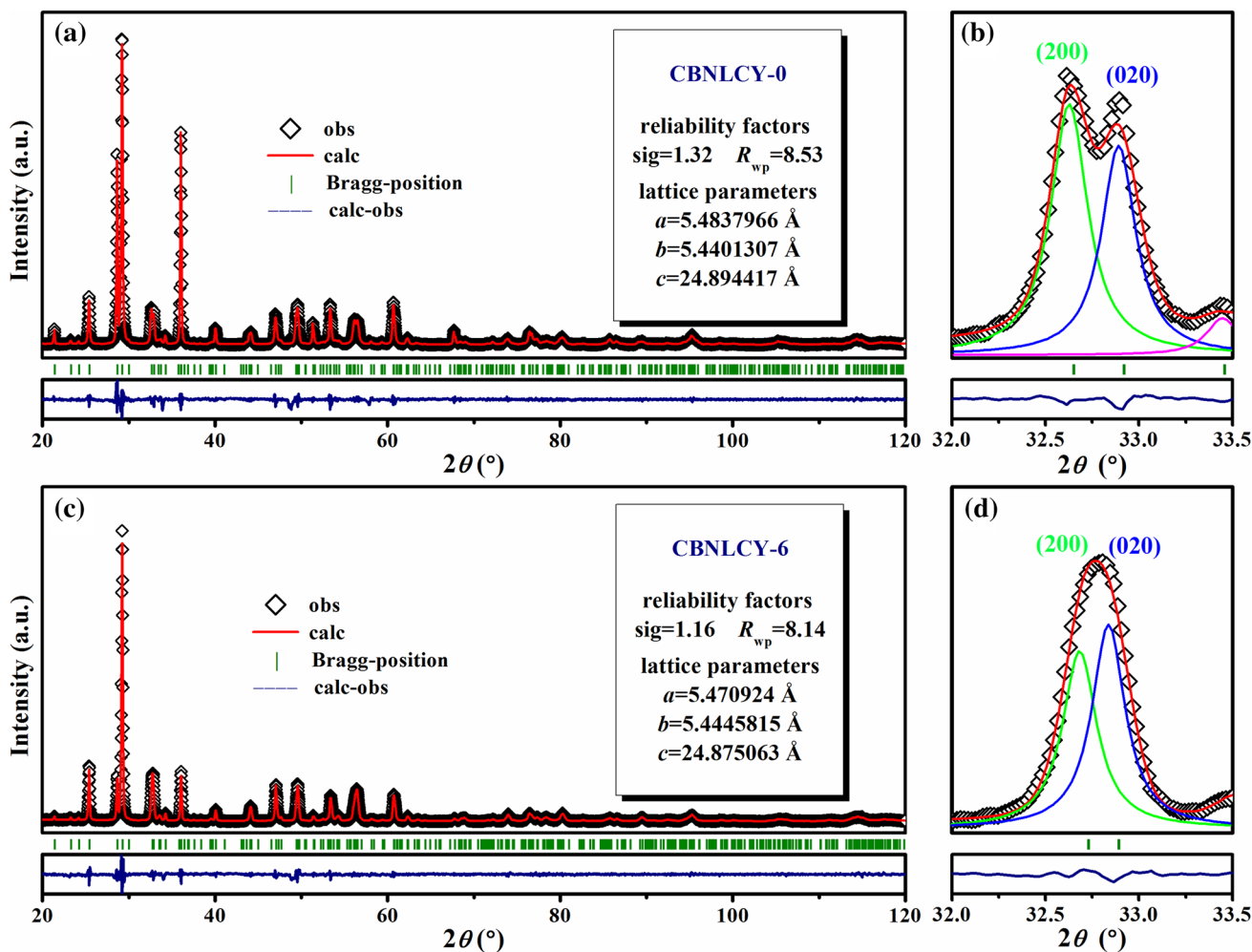
**Fig. 2** Rietveld refinement on powder XRD patterns of **a** CBNLCY-0 and **c** CBNLCY-6; **b, d** are enlarged XRD patterns located at (200)/(020)

the fatigue characteristics of CBNLCY-6 ceramics for $10^5$ switching cycles at 180 °C. The value of $P_r$ do not change obviously indicating that the CBNLCY-6 ceramic have good fatigue resistance.

The electric resistivity is an important factor of BLSFs ceramics, which should be considered for piezoelectric ceramics applied in high temperature. The temperature dependence of resistivity of CBNLCY-100$x$ ceramics are shown in Fig. 6a. The resistivity gradually declines with the increasing temperature as same as other Aurivillius type ceramics. Besides, the resistivity of CBNLCY-100$x$ ceramics increases with enhancement of the $x$ value and reaches the optimal value at $x = 0.01$ shown in Fig. 6b. The resistivity of CBNLCY-1 ceramics is $1.31 \times 10^6$ $\Omega \cdot$cm at 600 °C, which enhances one order of magnitude compared with undoped CBN ceramics ($1.25 \times 10^5$ $\Omega \cdot$cm at 600 °C). In general, the oxygen vacancies make a major contribution to the electric conduction process for Aurivillius type ceramics [29–31]. Due to the volatilization of bismuth element during sintering, there are bismuth

vacancies ($V_{Bi}'''$) leaving at the $(Bi_2O_2)^{2+}$ layer of CBNLCY-0 ceramics, and the oxygen vacancies ($V_O^{\cdot\cdot}$) are also generated near them to maintain the charge neutrality (Eq. 1). In the cooling process, the oxygen atoms enter into $(Bi_2O_2)^{2+}$ layer again and produce the holes ($h^{\cdot}$) (Eq. 2). The substitution of donor dopant $Ce^{4+}$ for $Ca^{2+}$ generates two electrons at A-site (Eq. 3), and neutralizes the holes (Eq. 4). Thus, the concentration of charge carriers of CBNLCY-100$x$ ceramics decreases when $x$ value is 0.01 mol, which makes the resistivity raise. The donor doping process can be represented by Kroger–Vink defect-chemical equation [32]:
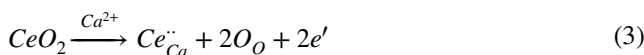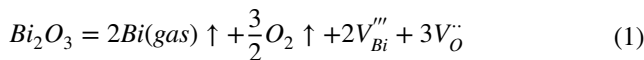
$$Bi_2O_3 = 2Bi(gas) \uparrow + \frac{3}{2}O_2 \uparrow + 2V_{Bi}''' + 3V_O^{\cdot\cdot} \tag{1}$$

$$V_O^{\cdot\cdot} + \frac{1}{2}O_2 \rightarrow O_O + 2h^{\cdot} \tag{2}$$

$$CeO_2 \xrightarrow{Ca^{2+}} Ce_{Ca}^{\cdot\cdot} + 2O_O + 2e' \tag{3}$$

**Fig. 3** Visualized crystal structures and bond distances of **a** CBNLCY-0 and **b** CBNLCY-6
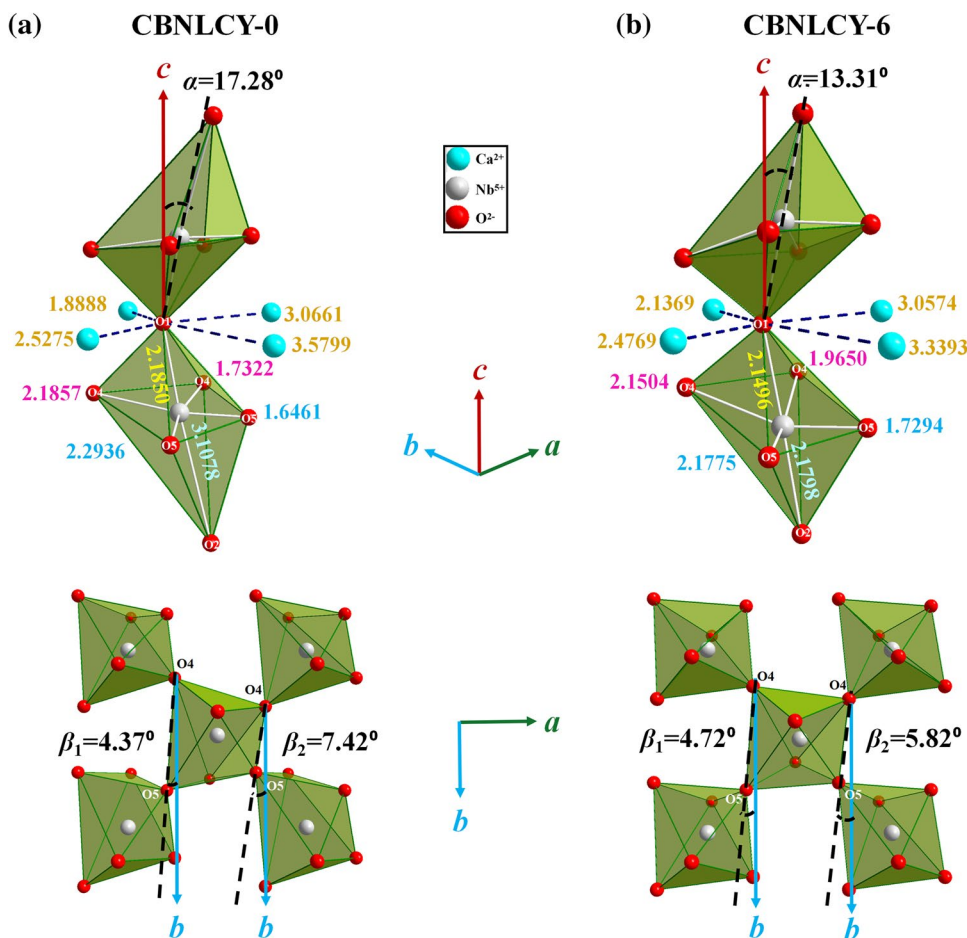


**Table 2** Summarization of the tilt angle ($\alpha$) of the octahedron from the $c$ axis, the tilt in the $a$–$c$ plane ($\alpha_x$) and in the $b$–$c$ plane ($\alpha_y$), and the octahedral rotation angle ($\beta_1$ and $\beta_2$) along the $b$ axis in the $a$–$b$ plane

| Sample | CBNLCY-0 | CBNLCY-6 |
|---|---|---|
| $\alpha$ (°) | 17.28 | 13.31 |
| $\alpha_x$ (°) | 1.03 | 15.82 |
| $\alpha_y$ (°) | 54.91 | 46.19 |
| $\beta_1$ (°) | 4.37 | 4.72 |
| $\beta_2$ (°) | 7.42 | 5.82 |

$$h^{\cdot} + e' \rightarrow null \tag{4}$$

With the further increase of $x$ value, the resistivity of CBNLCY-100$x$ ceramics decreases. It is reported that the lanthanide metals $Ce^{4+}$ also have chance to entered into B-site of the perovskite structure to replace the $Nb^{5+}$ because of their similar ionic radii ($R_{Ce}^{4+} = 0.87$ Å, $R_{Nb}^{5+} = 0.64$ Å, 6 CN) [33]. When the low valence $Ce^{4+}$ ions enter into B-site to replace $Nb^{5+}$ ions, one oxygen vacancy ($V_O^{\cdot\cdot}$) will be generated at B-site of perovskite layer [34]. The Kroger–Vink defect-chemical equation of acceptor doping process are

shown in Eq. (5). Hence, the concentration of charge carriers increases and makes the resistivity reduce.

$$CeO_2 \xrightarrow{Nb^{5+}} Ce'_{Nb} + 2O_O + \frac{1}{2}V_O^{\cdot\cdot} \tag{5}$$
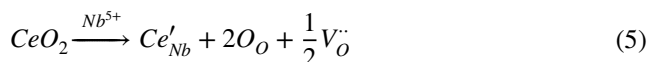
Furthermore, the temperature-dependent conduction process follows the Arrhenius equation [35]:

$$\rho = \rho_0 e^{\frac{E_a}{kT}} \tag{6}$$

where $\rho_0$ is the pre-exponential factor, $E_a$ is the activation energy of the charge carriers, $k_B$ is the Boltzmann's constant and $T$ is the absolute temperature. It can be seen that all curves can be divided into two temperature regions. The value of $E_a$ at low temperature is close to 1 eV, which is attribution to the motion of oxygen vacancy [36]. And at high temperature, the values of $E_a$ are near half of the band gap (1.7 eV), proving intrinsic conduction is the main conduction mechanism [37]. When $x$ value is 0.01 mol, the $E_a$ of CBNLCY-100$x$ ceramics has a slight decrease at low temperature but an increase at high temperature, which is ascribed to the decreasing concentration of oxygen vacancies. While with the $x$ content further increasing, it can be
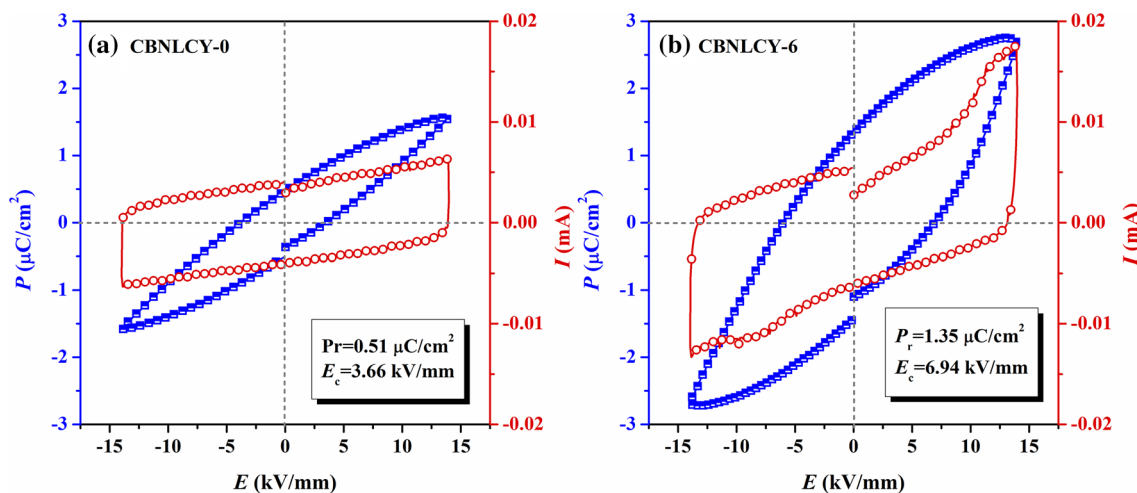
**Fig. 4** *P–E* loops and *I–E* curves of **a** CBNLCY-0 and **b** CBNLCY-6 ceramics measured at 180 °C and 1 Hz
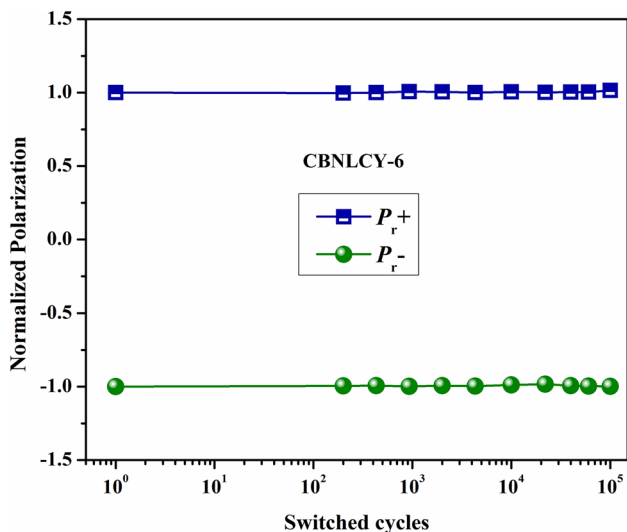


**Fig. 5** Fatigue characteristics of the CBNLCY-6 ceramics for $10^5$ switching cycles at 180 °C

observed that the activation energy increases at low temperature while declines at high temperature, and the values of $E_a$ in two temperature regions are both tend to 1 eV. It demonstrates that the $Ce^{4+}$ ions enter into B-sites and generate more oxygen vacancies. The schematic in Fig. 7 explains the defect formation process of the CBNLCY-100$x$ ceramics in detail. This result is consistent with the analysis of the variation of resistivity.

Figure 8a shows the temperature dependence of dielectric constant ($\varepsilon_r$) of the CBNLCY-100$x$ ceramics measured at 1 MHz. The dielectric peaks around 940 °C are the phase transition points between ferroelectric and paraelectric phase. The Curie temperature ($T_C$) of CBNLCY-100$x$ ceramics increases firstly with $x$ content increasing while decreases

with the further doping. In order to further elucidate the effect of LiCeY co-substitution on $T_C$, the tolerance factor ($t$) of the perovskites is invoked [12]. The formula of tolerance factor ($t$) is given by Eq. (7):

$$t = \frac{R_A + R_O}{\sqrt{2}(R_B + R_O)} \tag{7}$$

where $R_A$, $R_B$, and $R_O$ are the radii of A, B-site and oxygen atoms, respectively. In a certain range, the lower $t$ value often causes higher $T_C$. Compared with $Ca^{2+}$ ion ($R_{Ca}^{2+} = 1.34$ Å, 12 CN), the $Li^+$, $Ce^{4+}$ and $Y^{3+}$ ions ($R_{Li}^+ = 1.15$ Å, $R_{Ce}^{4+} = 1.14$ Å, $R_Y^{3+} = 1.25$ Å, 12 CN) have smaller radii which lead a lower $t$ value. So the $T_C$ presents an uptrend with $x$ content increasing and reaches the highest $T_C$ value (949 °C) at $x = 0.02$. Meanwhile, excessive LiCeY makes the crystal symmetry enhanced, resulting in a decrease of $T_C$ when $x \geq 0.02$. It is clear that the dielectric loss (tan$\delta$) of CBNLCY-100$x$ ceramics below 600 °C is flat, but increase rapidly near Curie points because of the movement of domain walls. Figure 8d shows the variation of tan$\delta$ with the $x$ value increasing at 600 °C. It is found that the CBNLCY-100$x$ ceramics obtain the lowest dielectric loss at $x = 0.01$. With the addition of less LiCeY ($x = 0.01$) into A-site, the oxygen vacancies generated by the volatilization of bismuth are neutralized by high valence $Ce^{4+}$ ions, which result in the lower dielectric loss [38].

Piezoelectric coefficient ($d_{33}$) and its thermal stability of CBNLCY-100$x$ ceramics are important parameters for high Curie temperature piezoceramics. Figure 9a shows the piezoelectric constant $d_{33}$ of CBNLCY-100$x$ ceramics at room temperature. As shown, the $d_{33}$ value increases and then stays nearly constant with the increase of the LiCeY content. The optimal piezoelectricity is obtained at $x = 0.06$ with a $d_{33}$ value of 16.3 pC/N, which is much larger than
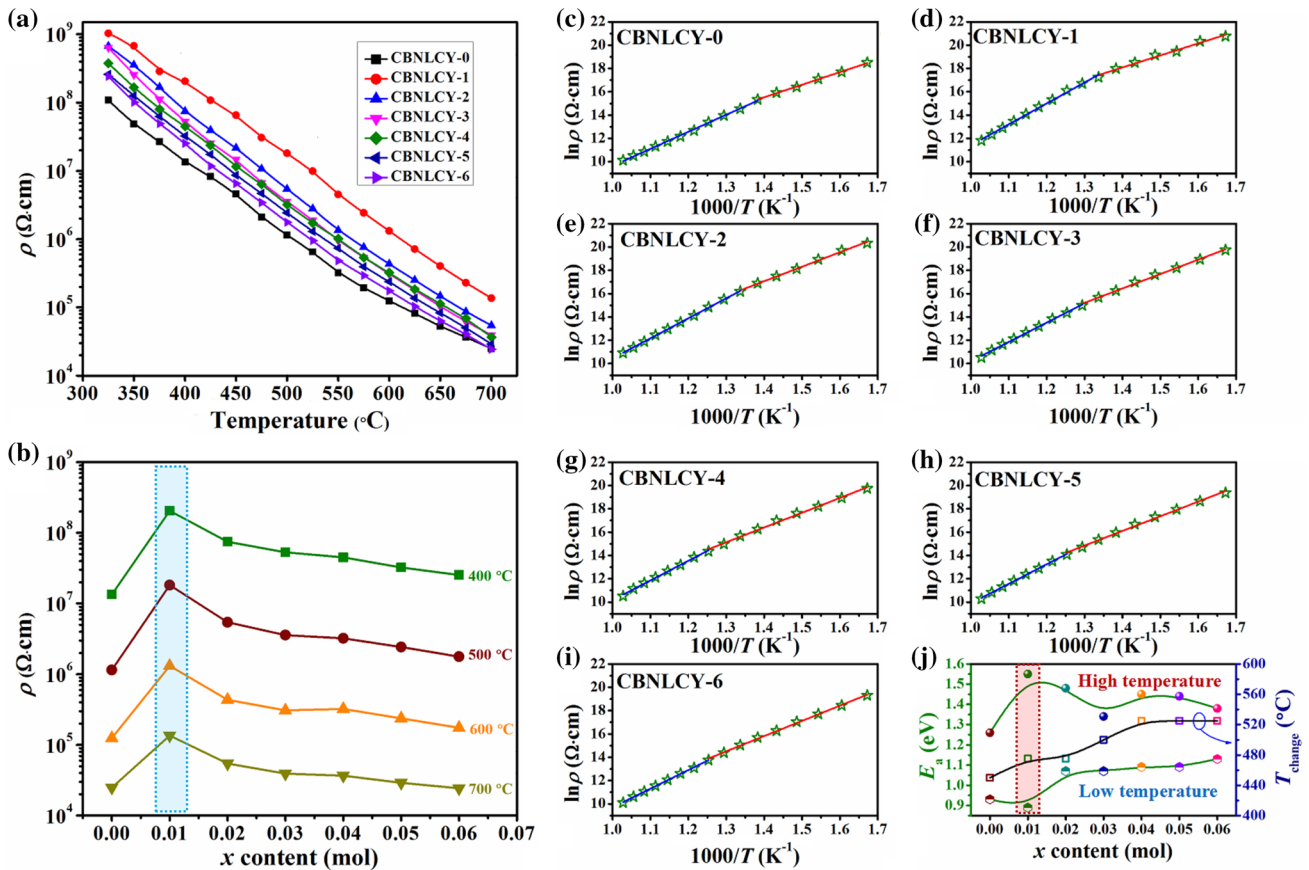
**Fig. 6 a** Resistivity of CBNLCY-100$x$ ceramics as a function of measuring temperature; **b** resistivity as a function of $x$ for CBNLCY-100$x$ ceramics at 400, 500, 600 and 700 °C; **c–i** Arrhenius relationship between $dc$ resistivity and temperature for the CBNLCY-100$x$ ceramics; **j** activation energy ($E_a$) obtained from the Arrhenius plots and the transition temperature $T_{change}$ corresponding to the changes of $E_a$



**Fig. 7** schematic of the defect formation process of CBNLCY-100$x$ ceramics
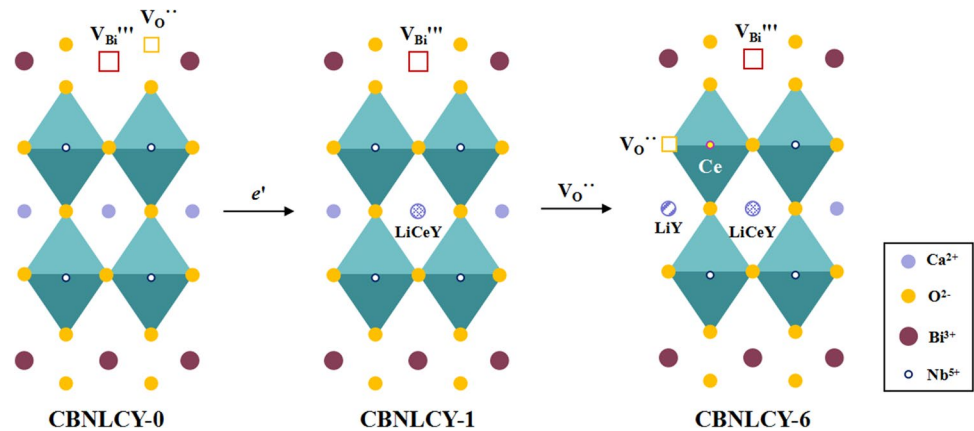
that of undoped CBN ceramics ($d_{33} = 6.6$ pC/N). The crystal distortion can explain the great enhancement of $d_{33}$ value. It has been studied that the octahedral tilt angle in the $a–c$ plane ($\alpha_x$) is the main contribution to the ferroelectricity of CBNLCY-100$x$ ceramics [28]. Compared with CBN-LCY-0 ceramic, CBNLCY-6 ceramic has larger $\alpha_x$ value,

and CBNLCY-6 ceramic also has larger remnant polarization $P_r$ shown in Fig. 4. Therefore, the CBNLCY-6 ceramic obtained the high piezoelectric constant. Figure 9b shows the thermal stability of CBNLCY-100$x$ ceramics. One could see that all the samples have stable piezoelectric properties. The $d_{33}$ value drops slightly when the annealing temperature
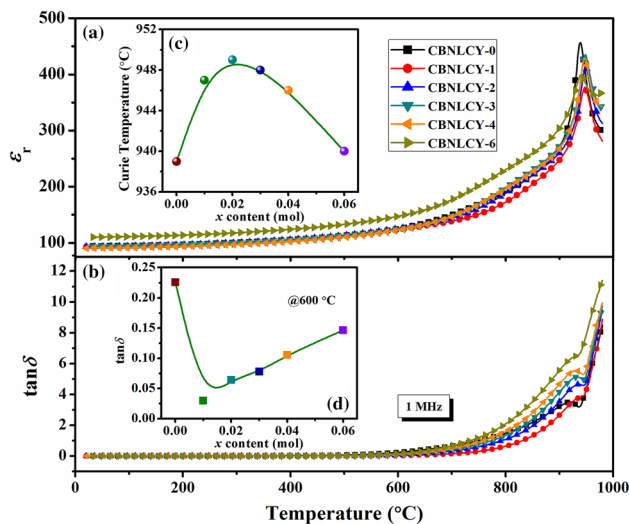
**Fig. 8** Temperature dependence of **a** dielectric constant ($\varepsilon_r$) and **b** dielectric loss (tan$\delta$) of the CBNLCY-100$x$ ceramics measured at 1 MHz. **c** The Curie temperature ($T_C$) as a function of the $x$. **d** shows tan$\delta$ as a function of $x$ at 600 °C

rises to 400 °C, which is attribution to the movement of non-180° domain walls [21, 39]. When the annealing temperature is close to Curie temperature, the $d_{33}$ value decreases rapidly, indicating the phase transition from ferroelectric phase to paraelectric phase. Figure 9c gives the relative $d_{33}$ of CBNLCY-6 ceramic after annealing at various temperatures. It is observed that the relative $d_{33}$ value of CBNLCY-6 ceramics still remains 92.6% of its original value, which indicates the CBNLCY-6 ceramic has good resistance to thermal aging.

# 4 Conclusions

The (LiCeY) co-doped $Ca_{1-2x}(LiCe_{0.5}Y_{0.5})_xBi_2Nb_2O_9$ (CBNLCY-100$x$, $x = 0$–0.07) ceramics were prepared by the conventional solid-state reaction. The substitution of (LiCeY) at A-site led an improvement of the octahedral tilt angle in the $a$–$c$ plane of CBNLCY-100$x$ ceramics, which resulted in an enhanced piezoelectric property. CBNLCY-6 ceramic with high Curie temperature ($T_C = 940$ °C) had an enhanced piezoelectric coefficient ($d_{33}$) of 16.3 pC/N. Even after annealing at 800 °C for 2 h, the $d_{33}$ value of CBNLCY-6 ceramic still remained 92.6% of its original value. Furthermore, detailed investigations about the resistivity of CBNLCY-100$x$ ceramics showed that the oxygen vacancies played an important role in $dc$ conduction mechanism at low temperature and the main conduction mechanism at high temperature was intrinsic conduction. The high valence state ions $Ce^{4+}$ entered into A-site of perovskite to reduce the concentration of oxygen vacancies, finally enhanced the resistivity of CBNLCY-100$x$ ceramics and decreased the dielectric loss. But with the further modification, the $Ce^{4+}$ might enter into B-site as an acceptor and generated more oxygen vacancies. Ultimately, CBNLCY-1 ceramic got the highest resistivity ($1.31 \times 10^6$ Ω cm) and lowest tan$\delta$ (~0.03) at 600 °C.



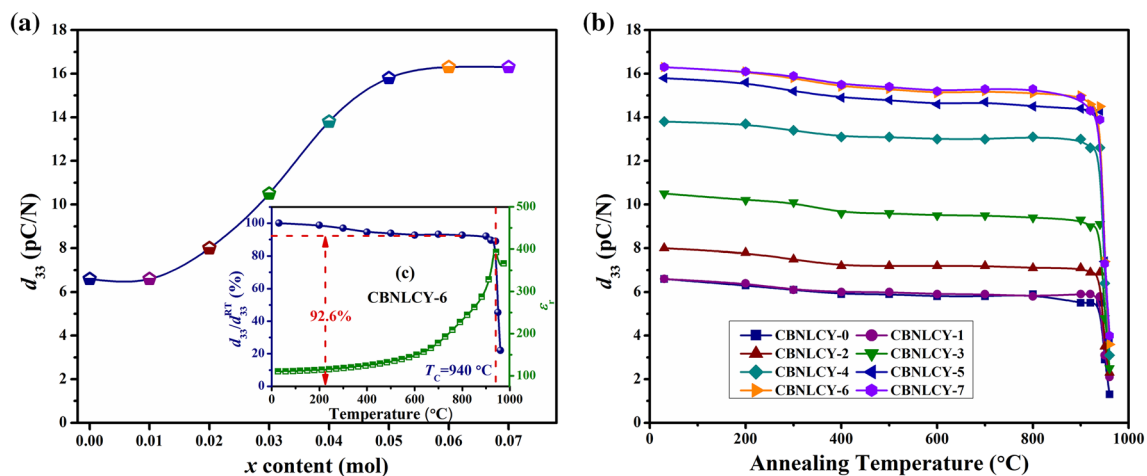**Fig. 9** **a** Piezoelectric coefficient $d_{33}$ of CBNLCY-100$x$ ceramics at room temperature; **b** thermal depoling behavior of CBNLCY-100$x$ ceramics; **c** the relative $d_{33}$ after annealing at various temperatures and temperature dependent dielectric constant $\varepsilon_r$ of CBNLCY-6 ceramic

# References

1. S.M. Blake, M.J. Falconer, M. Mccreedy, P. Lightfoot, J. Mater. Chem. **7**, 1609 (1997)
2. H. Chen, B. Shen, J. Xu, L. Kong, J. Zhai, J. Am. Ceram. Soc. **95**, 3514 (2012)
3. C.M. Wang, S. Zhang, J.F. Wang, M.L. Zhao, C.L. Wang, Mater. Chem. Phys. **118**, 21 (2009)
4. E.C. Subbarao, J. Phys. Chem. Solids **23**, 665 (1962)
5. E.C. Subbarao, J. Am. Ceram. Soc. **45**, 166 (1962)
6. X. Zhang, H. Yan, M.J. Reece, J. Am. Ceram. Soc. **91**, 2928 (2008)
7. X.X. Tian, S.B. Qu, H.L. Du, Y. Li, Z. Xu, Chin. Phys. B **21**, 037701 (2012)
8. Z. Peng, Q. Chen, Y. Wang, D. Xin, D. Xian, J. Zhu, Mater. Lett. **107**, 14 (2013)
9. C.M. Wang, J.F. Wang, S. Zhang, T.R. Shrout, Phys. Status Solidi RRL **3**, 49 (2009)
10. Y. Wang, J. Wu, Z. Peng, Q. Chen, D. Xin, D. Xiao, J. Zhu, Appl. Phys. A **119**, 337 (2015)
11. J. Xie, J. Zhong, C. Wu, Y. Shi, D. Wang, G. Liu, D. Liang, B. Wang, J. Zhu, Q. Chen, J. Am. Ceram. Soc. **00**, 1 (2018)
12. C. Long, H. Fan, M. Li, P. Ren, Y. Cai, Cryst. Eng. Commun. **15**, 10212 (2013)
13. G. Liu, J. Yuan, R. Nie, L. Jiang, Z. Tan, J. Zhu, Q. Chen, J. Alloy. Compd. **697**, 380 (2016)
14. Y. Chen, S. Xie, H. Wang, Q. Chen, Q. Wang, J. Zhu, Z. Guan, J. Alloy. Compd. **696**, 746 (2017)
15. C. Long, H. Fan, M. Li, Appl. Phys. Lett. **103**, 192908 (2013)
16. S.M. Ke, H.T. Huang, H.Q. Fan, H.K. Lee, L.M. Zhou, Y.W. Mai, Appl. Phys. Lett. **101**, 082901 (2012)
17. T. Li, H. Fan, C. Long, G. Dong, S. Sun, J. Alloy. Compd. **609**, 60 (2014)
18. Y. Guo, H. Fan, C. Long, J. Shi, L. Yang, S. Lei, J. Alloy. Compd. **610**, 189 (2014)
19. H. Chen, J. Zhai, J. Electron. Mater. **41**, 2238 (2012)
20. J. Liu, Z. Shen, M. Nygren, Y. Kan, P. Wang, J. Eur. Ceram. Soc. **26**, 3233 (2006)
21. C. Long, H. Fan, M. Li, Dalton Trans. **42**, 3561 (2013)
22. R.D. Shannon, Acta Crystallogr. Sect. A Found. Adv. **32**, 751 (1976)
23. Y. Wu, J. Chen, J. Yuan, J. Xing, Z. Tan, L. Jiang, Q. Chen, J. Zhu, J. Appl. Phys. **120**, 194103 (2016)
24. L. Xie, J. Xing, Z. Tan, L. Jiang, Q. Chen, J. Wu, W. Zhang, D. Xiao, J. Zhu, J. Alloy. Compd. **758**, 14 (2018)
25. J. Yuan, J. Chen, S. Bao, Q. Chen, D. Xiao, J. Zhu, J. Mater. Sci. Mater. Electron. **29**, 21051 (2018)
26. Z. Peng, X. Xing, X. Zeng, Y. Xiang, F. Cao, B. Wu, Mater. Res. Bull. **97**, 393 (2018)
27. Y. Noguchi, M. Miyayama, T. Kudo, Phys. Rev. B **63**, 214102 (2012)
28. Z.G. Yi, Y. Wang, Y.X. Li, Q.R. Yin, J. Appl. Phys. **99**, 114101 (2006)
29. H. Chen, X. Guo, Z. Cui, J. Zhai, Phys. Status Solidi A **210**, 1121 (2013)
30. J. Chen, J. Yuan, S. Bao, Y. Wu, G. Liu, Q. Chen, D. Xiao, J. Zhu, Ceram. Int. **43**, 5002 (2017)
31. C. Long, H. Fan, Y. Wu, Y. Li, J. Appl. Phys. **116**, 074111 (2014)
32. Z. Peng, Y. Chen, Q. Chen, N. Li, X. Zhao, C. Kou, D. Xiao, J. Zhu, J. Alloy. Compd. **590**, 210 (2014)
33. Y. Tsur, T.D. Dunbar, C.A. Randall, J. Electroceram. **7**, 25 (2001)
34. Z. Peng, Q. Chen, D. Liu, Y. Wang, D. Xiao, J. Zhu, Curr. Appl. Phys. **13**, 1183 (2013)
35. Z. Zhou, X. Dong, H. Chen, H. Yan, J. Am. Ceram. Soc. **89**, 1756 (2006)
36. Z. Zhou, X. Dong, H. Yan, H. Chen, C. Mao, J. Appl. Phys. **100**, 044112 (2016)
37. Z. Peng, Q. Chen, Y. Chen, D. Xiao, J. Zhu, Mater. Res. Bull. **59**, 125 (2014)
38. Z. Peng, X. Xing, Y. Xiang, F. Cao, B. Wu, J. Alloy. Compd. **728**, 797 (2017)
39. Z. Peng, D. Yan, Q. Chen, D. Xin, D. Liu, D. Xiao, J. Zhu, Curr. Appl. Phys. **14**, 1861 (2014)